Surface Waves and Crustal Structure on Mars

D. Kim, W. Banerdt, S. Ceylan, D. Giardini, V. Lekić, Philippe Lognonné, C. Beghein, É. Beucler, S. Carrasco, C. Charalambous, et al.

Title: Surface Waves and Crustal Structure on Mars

Authors: D. Kim[1]*, W. B. Banerdt[2], S. Ceylan[1], D. Giardini[1], V. Lekic[3], P. Lognonné[4], C. Beghein[5], É. Beucler[6], S. Carrasco[7], C. Charalambous[8], J. Clinton[9], M. Drilleau[10], C. Durán[1], M. Golombek[2], R. Joshi[11], A. Khan[1,12], B. Knapmeyer-Endrun[7], J. Li[5], R. Maguire[13], W. T. Pike[7], H. Samuel[4], M. Schimmel[14], N. Schmerr[3], S. C. Stähler[1], E. Stutzmann[4], M. Wieczorek[15], Z. Xu[4], A. Batov[16], E. Bozdag[17], N. Dahmen[1], P. Davis[5], T. Gudkova[16], A. Horleston[18], Q. Huang[17], T. Kawamura[4], S. King[19], S. M. McLennan[20], F. Nimmo[21], M. Plasman[4], A. C. Plesa[22], I. E. Stepanova[16], E. Weidner[5], G. Zenhäusern[1], I. J. Daubar[23], B. Fernando[24], R. Garcia[9], L. V. Posiolova[25], M. P. Panning[2]

Affiliations:

[1]Institute of Geophysics, ETH Zürich, Zürich, Switzerland
[2]Jet Propulsion Laboratory, California Institute of Technology, Pasadena, CA, USA
[3]Department of Geology, University of Maryland, College Park, MD, USA
[4]Université de Paris, Institut de Physique du Globe de Paris, CNRS, Paris, France
[5]Department of Earth, Planetary and Space Sciences, University of California, Los Angeles, CA, USA
[6]Laboratoire de Planétologie et Géodynamique, UMR6112, Université de Nantes, Université dAngers, CNRS, Nantes, France
[7]Bensberg Observatory, University of Cologne, Bergisch Gladbach, Germany
[8]Department of Electrical and Electronic Engineering, Imperial College London, London, UK
[9]Swiss Seismological Service, ETH Zürich, Zürich, Switzerland
[10]Institut Supérieur de l'Aéronautique et de l'Espace SUPAERO, Toulouse, France
[11]Max Planck Institute for Solar System Research, Göttingen, Germany
[12]Physik-Institut, University of Zürich, Zürich, Switzerland
[13]Department of Computational Mathematics, Science, and Engineering, Michigan State University, East Lansing, MI, USA
[14]Geosciences Barcelona – CSIC, Barcelona, Spain
[15]Université Côte d'Azur, Observatoire de la Côte d'Azur, CNRS, Laboratoire Lagrange, Nice, France
[16]Schmidt Institute of Physics of the Earth, Russian Academy of Sciences, Moscow, Russia
[17]Department of Geophysics, Colorado School of Mines, Golden, CO, USA
[18]School of Earth Sciences, University of Bristol, Bristol, UK
[19]Department of Geosciences, Virginia Tech, Blacksburg, VA, USA
[20]Department of Geosciences, Stony Brook University, Stony Brook, NY, USA
[21]Department of Earth and Planetary Sciences, University of California Santa Cruz, Santa Cruz, CA, USA
[22]Institute of Planetary Research, German Aerospace Center (DLR), Berlin, Germany
[23]Department of Earth, Environmental, and Planetary Sciences, Brown University, Providence, RI, USA
[24]Department of Earth Sciences, University of Oxford, Oxford, UK
[25]Malin Space Science Systems, San Diego, CA, USA

*Corresponding author. Doyeon Kim (doyeon.kim@erdw.ethz.ch)

Abstract:

We detected surface waves from two meteoroid impacts on Mars. By measuring group velocity dispersion along the impact-lander path, we obtained a direct constraint on crustal structure away from the *InSight* lander. The crust north of the equatorial dichotomy has a shear wave velocity of ~3.2 km/s in the 5-30 km depth range, with little depth-variation. This implies a higher crustal density than inferred beneath the lander, suggesting either compositional differences or reduced porosity in the volcanic areas traversed by the surface waves. The lower velocities and the crustal layering observed in the landing site down to 10 km depth are not a global feature. Structural variations revealed by surface waves hold implications for models of the formation and thickness of the martian crust.

One-Sentence Summary:

Surface waves detected by *InSight* from two large meteoroid impacts reveal lateral variations in crustal structure of Mars.

Main Text:

The martian crust exhibits striking variations in topography, inferred thickness, age, cratering, resurfacing and volcanism (*1*). Constraining the variation of crustal properties and composition with depth is crucial for understanding its origin and evolution (*2*). Inferences of crustal thickness and density variations, which are derived from joint analysis of topography and gravity data, suffer from substantial trade-offs (*3*). For example, the ~5 km topographic difference between the highly-cratered southern highlands and the low-lying, less cratered northern plains can be explained by differences in crustal thickness or by large variations in crustal density (*4*) or a combination thereof.

The *InSight* mission to Mars (*5*) has provided direct constraints on the layering of Mars' crust at the landing site (*6*). Analyses of body wave conversions and ambient noise wavefield have constrained the crustal thickness beneath the *InSight* lander in Elysium Planitia to be 39±8 km (*7-9*), providing a key anchoring-point for global models of crustal thickness and density variations. Looking deeper, travel times of body waves from several marsquakes have enabled the determination of seismic velocity profiles of the upper mantle (*10*) and core radius (*8, 11*) and mean density (*12*). Despite these achievements, competing effects of epicentral distance, source depth, and radial structure on body wave travel times (*13*), have stymied efforts to constrain lateral variations in structure using a single seismometer on Mars.

The velocity of surface waves, unlike that of body waves, depends on frequency, with lower-frequency waves sensitive to greater depths. The measurement of surface wave dispersion therefore provides a direct observation of the depth-dependent variation of seismic velocities averaged along the path from source to receiver (*14*). Until now surface waves had not been observed on any marsquake records. Their absence could be due to the relatively small magnitude of the recorded seismic events (*15*), large source depths (*8*) and/or contamination of seismic data by long-period wind noise as well as atmospheric pressure waves (*16*). Strong crustal scattering on Mars (*6, 17*) can also impede the propagation and affect the visibility of surface waves, as was the case on the Moon (*18*).

We report here the first detection of surface waves on Mars, in the seismic waveforms of events S1094b and S1000a. S1094b, which occurred on December 24th, 2021, is the third-largest seismic event (Mw = 4.0±0.2) and has the longest-duration seismic signal recorded to date by InSight (*19*), with coda energy persisting for more than 135 minutes. Based on the differential

travel time of the direct P and S arrivals, and measured P-wave polarization, the initial distance and back azimuth estimates provided by the Marsquake Service were 59.7±6° and 40° (-9°, +18°), corresponding to a source region in Amazonis Planitia, ~3460 km northeast from InSight (Fig. 1). The Mars Reconnaissance Orbiter (MRO) images taken between December 24-25, 2021 reveal a large impact crater in Amazonis Planitia, 3532 km away from the lander and consistent with the source location estimated for S1094b (*20*). With similar broad frequency content and moment magnitude of S1094b, event S1000a has also been identified as atypical based on its seismic characteristics (*19*) and was recently associated with an impact crater near the Tharsis province, ~7460 km away from the InSight lander (*20*). The ground-truth identification of the two events as impacts removes all uncertainties related to hypocentral depth.

We apply standard marsquake data processing methodologies (*19*) to the S1094b waveform data. An unusually large amplitude seismic arrival is observed 800 s after the P-wave in the S-wave coda in the vertical-component spectrogram (Fig. 2). The arrival's frequency content is considerably lower than typical of P- and S-wave arrivals in low-frequency (LF) family marsquakes (*8, 10*). Narrow-band filter banks of the raw vertical-component data show dispersion in the 6-18 s period range (Fig. 2). Frequency-dependent polarization analysis confirms that particle motion is strongly elliptically-polarized in the vertical plane (fig. S1E). The systematic phase shift between the vertical and horizontal components suggests that the arrival has a predominantly retrograde particle motion and arrives from 51° due northeast, consistent with the polarization of the direct P-wave (fig. S5).

Taken together, these characteristics allow the positive identification of this phase as the minor-arc Rayleigh wave (R1). Although strong elliptical polarization has been previously observed in the 3-30 s period range of the ambient seismic noise recordings, they were strictly polarized in the horizontal plane (*17*) and correlated with daytime wind direction on Mars. Despite heavy late afternoon winds, a comodulation analysis of the potential wind injection during the R1 arrival documents excess seismic energy over that generated by wind between 8-15 s at the time of the observation (fig. S3). Moreover, we confirm that the seismic data recorded during the surface wave arrival is not contaminated by any known electro-mechanical artifacts associated with the seismic sensor or the InSight spacecraft system (*24*).

We find no evidence for Love waves in the S1094b records. This observation is consistent with an impact origin for S1094b, as an isotropic source would primarily excite Rayleigh waves. The detection of Rayleigh waves from this impact source, but not from other LF marsquakes, supports the argument that marsquakes recorded to date are generally too deep to effectively excite surface waves (*25*). Our waveform simulation confirms that surface waves from shallow seismic sources are far more likely to be detectable, given the diurnal ambient noise level on Mars (fig. S14).

We observed an additional anomalous seismic arrival approximately 75 minutes after the identified R1 (fig. S2). Like for the R1 observation, the time of this arrival is far outside the time window for a potential direct or ground-coupled infrasound wave originating from the impact source region (*20, 26*). However, the timing is consistent with that expected for the major-arc Rayleigh wave (R2), that propagated in the opposite direction around Mars. Dispersion and enhanced elliptical polarization in the vertical plane in the 6-11 s period range supports the R2 interpretation. While the frequency content of this arrival is comparable to that of R1, broadband environmental injection in the analysis window is also evident (fig. S4). Due to low signal-to-noise ratio, the direction of propagation and particle motion of this phase are unclear and thus the

identification of R2 is not definitive. We find no evidence for the arrival of surface wave overtones, nor multi-orbiting Rayleigh waves in the S1094b waveforms (*19*).
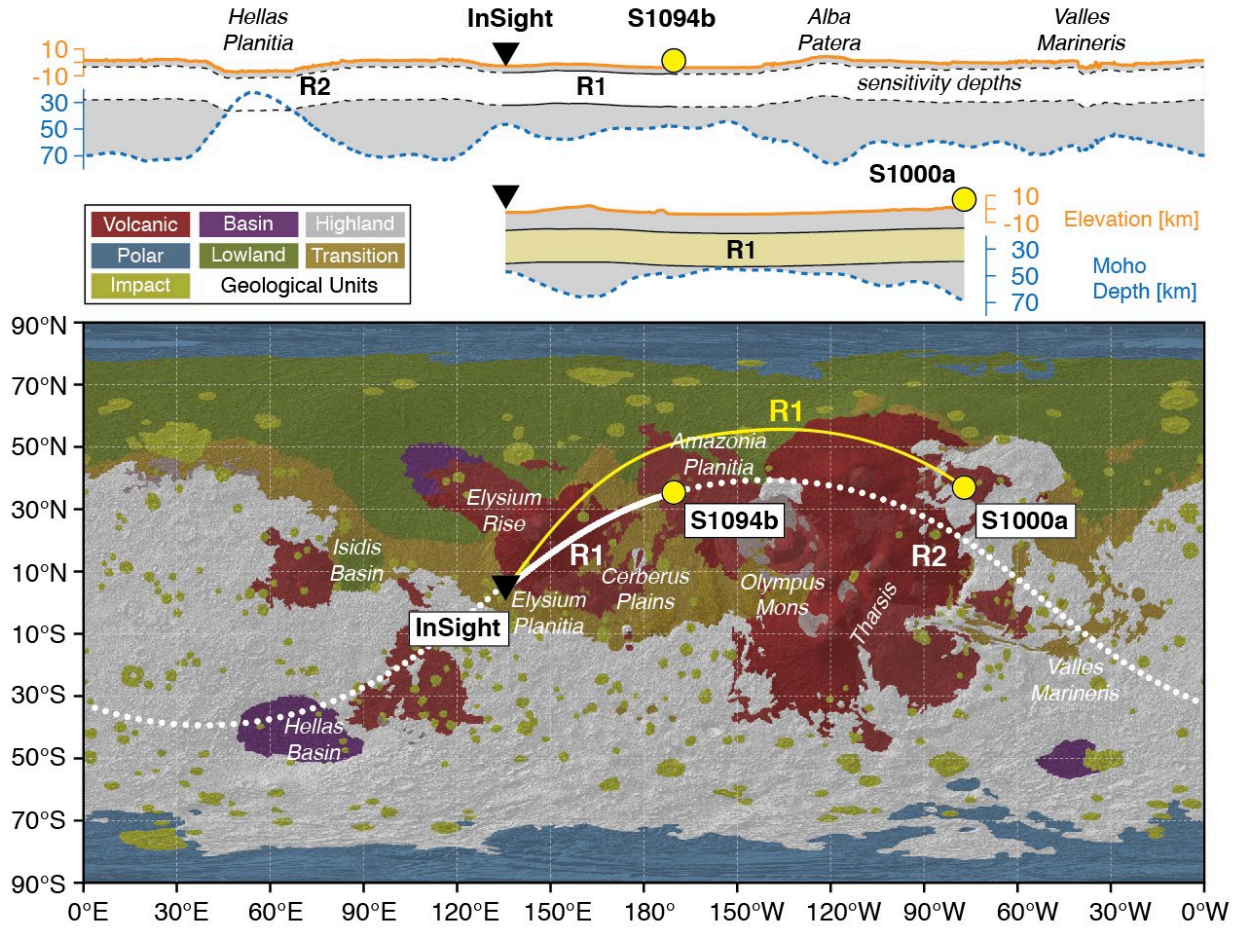

Figure 1. Locations of two large meteoroid impacts (yellow circles) identified in MRO images (*20*). The great circle paths for R1 (solid) and R2 (dashed) in S1094b are in white, while the R1 path for S1000a is in yellow. Background topographic relief is from the Mars Orbiter Laser Altimeter (*21*). The distribution and sequence of major geological unit groups of Hesperian and Amazonian age (*22*) are overlaid. Global elevation (orange) and the crust-mantle boundary depth profiles (*23*) along the R1 and R2 paths (dashed blue) are shown at the top.
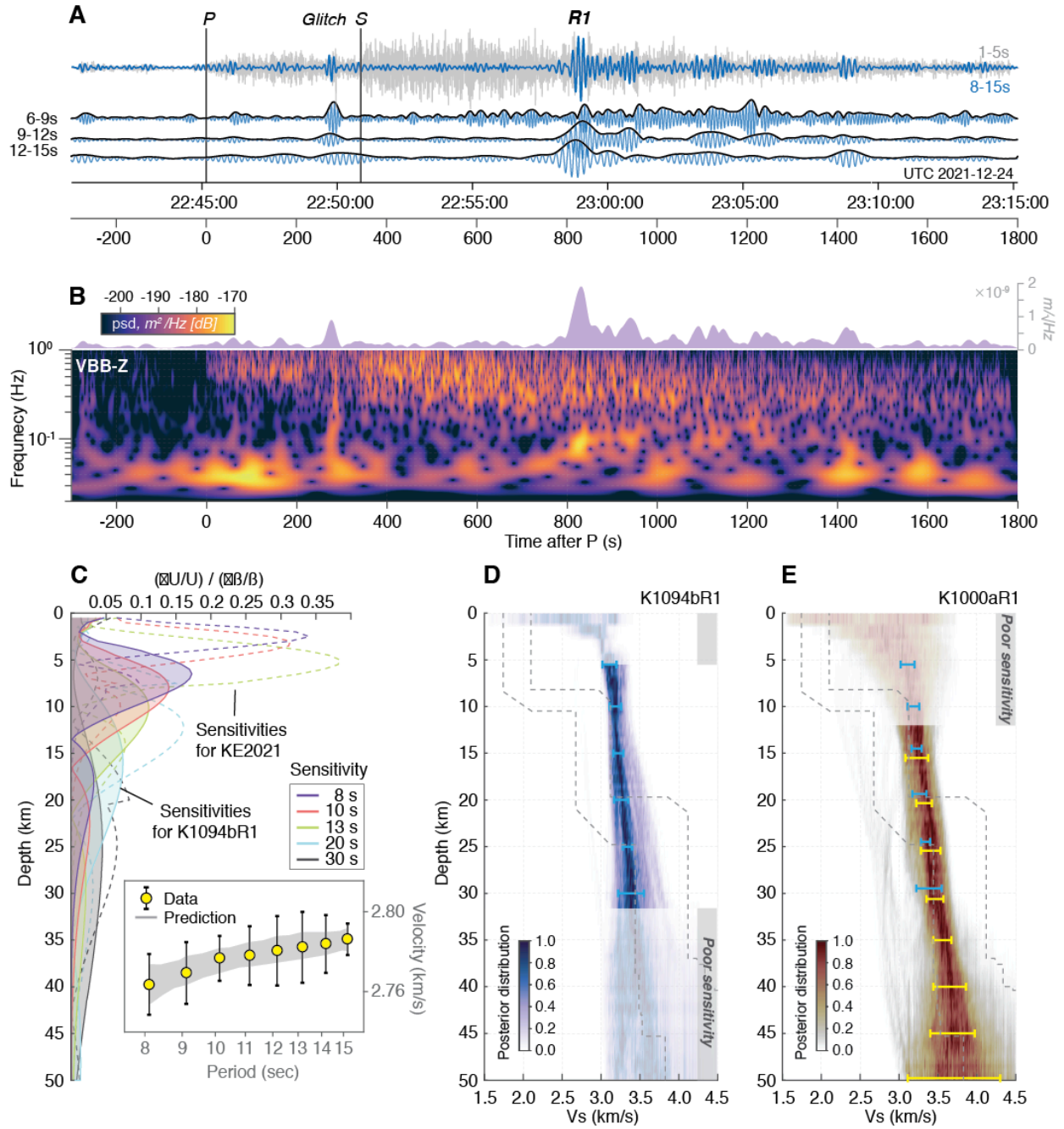
5

Figure 2. Seismic waveforms and velocity profiles. (**A**) Vertical-component seismogram of S1094b bandpass filtered between 1-5 s (gray) and 8-15 s (blue) with P and S wave picks (black vertical lines). Narrow-band filter banks and envelopes show dispersed signals 800 s after the P-wave. (**B**) The vertical component S-transform shows a large amplitude seismic arrival that exhibits dispersion (c.f., 2A). The frequency domain envelope averaged across the 8-15 s period range is plotted at the top of the spectrogram. Other characteristics enabling the identification of this dispersive arrival as R1 are shown in the Supplementary Materials (*19*). (**C**) Depth sensitivity kernels and data misfit of R1 in S01094b (inset). The mean and standard deviation are drawn from 10 pairs of dispersion measurements (fig. S6). Kernels in dashed lines are computed based on the three-layer crustal model in (*7*) denoted as KE2021. Note the substantial differences between the kernels due to different velocity profiles. Shaded kernels and predictions are computed using the average model in panel 2D. (**D**) Posterior distribution of V_S structure inverted from the group velocity measurements of S1094b R1 (K1094bR1). Posterior distribution and prediction are based on the best-fitting 10,000 models after one million iterations. Depths where sensitivity is inadequate (<40% in cumulative kernel strength) are muted. The range of V_S in the three-layer crustal models beneath the lander (*7*) are indicated by gray

dashed lines. (**E**) Posterior distribution of the V_S structure inverted with the group velocity measurements of the potential S1000a R1 (K1000aR1) at ~20 s and ~30 s period (fig. S12).

Surface wave data on Earth are typically interpreted assuming that propagation occurs along the great circle path from source to receiver, and that it can be related to the average flat-layer structure along that path (*27*). Using a number of crustal thickness models constructed based on gravimetric data and the extrapolated crustal thickness estimates from the InSight location (*23*), our kinematic ray tracing predicts negligible deviations from great circle paths for R1 and R2, less than 0.2% of the total travel time (*19*). We measured the group velocities of R1 and R2 and obtained average values of 2.77 and 3.14 km/s, respectively, which imply structural differences along their propagation paths (fig. S6). Indeed, while the R1 path traverses only the northern lowlands, a large fraction of the R2 path crosses the southern highlands and between 12% and 17% of the path passes through the Hellas impact basin, where the crust has been largely removed and replaced by uplifted mantle (*28*). Consequently, the crustal thickness within the Hellas impact basin could be as low as a few kilometers (*23*) and R2 would travel at seismic velocities characteristic of the uppermost mantle (V_S 4-4.5 km/s) at periods of 10-16 s. The observed higher value in the average group velocity of R2 with respect to R1 could then be accounted for by Hellas alone and as a result the average crustal velocity of the southern and northern hemispheres would be very similar (fig. S18).

Notably, both phases show little dispersion in the observed frequency range, which is primarily sensitive to crustal structure between ~5-30 km depth (Fig. 2C). We inverted for path-averaged radial P- and S-wave velocity profiles using the R1 measurements with multiple approaches (Fig. 2C, and figs. S8-S10) and regardless of the parameterization strategies considered (*19*), we obtained a uniform V_S of about 3.2 km/s, with a slight linear increase down to 30 km depth. At greater depths, we lose sensitivity due to lack of dispersion measurements at long periods (Fig. 2). At shallowest depths, we cannot rule out a thin slow layer, though due to the non-linear relationship between V_S profiles and surface wave sensitivity kernels (Fig. 2C), the greatest permissible thickness of such a layer depends on its V_S. The uniform V_S in the 5-30 km crustal depth range is different from the three-layer crustal structure observed beneath InSight (*7-9*). The obtained V_S is substantially higher in the upper 10 km and is similar to the average velocities of the second and third layers beneath the lander (Fig. 2D), but does not show the same velocity jump around 20 km depth. From the comparison of the local and the R1 path-average velocity structures, we conclude that the low-velocity observed down to 8-10 km depth below the lander is a local feature and if present in other parts along the path it must be restricted to only few kilometers below the surface. We cannot exclude the presence of deeper layering in the crust, but this would have to occur at varying depths along the path, to be averaged in the observed linear V_S increase with depth.

The high crustal seismic velocities inferred from the S1094b dispersion analysis are supported by S1000a data. Two distinct long-period arrivals, at ~20 s and ~30 s periods, are visible in the vertical-component spectrogram of S1000a in the R1 group arrival time range predicted based on the posterior distribution on V_S (fig. S11). While R1 in S1094b shows clear polarization, the comparative strength of the environmental injection during the expected R1 window of S1000a prevents a definitive identification. The inferred V_S structure using the S1000a group velocity measurements at ~20 s and ~30 s periods (2.73 km/s and 2.83 km/s) overlaps with our posterior V_S distribution based on group velocities of R1 for S1094b down to 30 km depth and provides additional constraints to image a slowly increasing V_S in the lower crust down to 45 km depth (Fig. S2E). This agreement suggests a high degree of similarity in the average crustal structure along the two R1 paths

Unlike dispersion, the frequency-dependence of Rayleigh wave ellipticity, expressed as the ratio of horizontal-to-vertical amplitude (H/V), is strongly sensitive to the structure directly beneath InSight. We find that the H/V measurements made on R1 are consistent with previous models of crustal layering directly beneath InSight (figs. S15, S16), as are P-to-s conversions in the P-wave coda of S1094b which show prominent arrivals at 2.4 s, 4.8 s, and 7.2 s after the direct P arrival (fig. S19, S20). Even with a single event, we can confirm that the shallow crustal structure at the landing site down to 10 km depth is substantially slower than the average crustal velocity sampled by the R1 path.

The observed surface waves allow us to expand the current understanding of crustal structure on Mars beyond the crustal layering inferred beneath the InSight landing site (*7*). We find that the low V_S layer extending down to 10 km depth in the shallow crust of Elysium Planitia does not exist globally on Mars. Instead, the average crustal velocities along the R1 paths of S1000a and S1094b (Fig. 3) are considerably faster and are likely to be more representative of average crustal structure. Large geographic variations in upper crustal structure hold implications for interpreting waveforms of surface-bouncing seismic waves such as PP and SS, and must be explicitly accounted for when constructing models of the spherically-symmetric structure of Mars. Relatedly, these structural variations hold clues for the deeper signature of surface geologic units and for interpretations of gravity data.

A large portion of the R1 paths between Elysium and Amazonis Planitiae passes through the Elysium rise, the largest volcanic province in the northern lowlands (Fig. 1). Its surface geology is characterized by lava flows of Hesperian to Amazonian age, reaching up to several kilometers of thickness and representing a history of major resurfacing (*29*). Beyond Elysium, the S1000a R1 path again encounters extensive regions covered by Hesperian and Amazonian volcanics in Amazonis Planitia and north of Alba Patera. Differently, the plains around the InSight lander are composed of Early Hesperian and Early Amazonian lava flows (*30, 31*) whose limited thickness is insufficient to affect R1 dispersion. Below ~200 m, weaker sedimentary material is suggested to extend in places at least to 5-6 km depth based on the phyllosilicate signatures and layered sedimentary rocks brought up in the central peaks of large impact craters (*32*).

Similar constraints are provided by density inferred from gravity data. The maximum permissible density of the overall crust on Mars (2850-3100 kg/m^3) is lower than the density of most martian basaltic materials found at the surface, as estimated by gamma-ray compositional mapping (*33*) and by mineralogical norms for SNC meteorites of predominantly Amazonian age (see summary in *23*). The two factors contributing to a layered crustal density structure on a global scale could be a less mafic (less dense) composition and/or an elevated porosity (*6, 7, 23*) (Fig. 3).

As most of the R1 paths pass through regions resurfaced by relatively young volcanic rocks, this would result in similar, higher densities of the upper and lower crust. Although Elysium volcanic cumulates are only a few kilometers thick (*22*) and thus within the uppermost zone of poor seismic sensitivity (Fig. 2), their magmatic history influenced the nature of the whole crust in this region (*34, 35*). The average ratio of intrusive/extrusive magmatism on Mars (*36, 37*) implies that intrusives account for >5 km of average crustal thickness integrated over the entire Elysium rise, and even more near the volcanic centers traversed by R1 (Fig. 1). One proposal for Mars is that intrusive rocks (i.e. magma chamber centers) would concentrate at greater depths than on Earth (*34*). These intrusive magmas represent, at least in part, residues of the partial melting giving rise to surface lavas and so likely are of greater density (*38*) and elevated seismic wave speeds closer to values typical of basaltic volcanic rocks, consistent with the path-average velocity profiles we observe below 5 km depth (Fig. 2).

Substantial porosity is also likely to be present in the upper crustal layers beneath the lander (*6, 7, 23*). Their low V_S is compatible with fractured basalt having, for example, 10% porosity, though the exact amount depends strongly on both the aspect ratio of the pore spaces and material contained therein (fig. S21). However, the higher path-averaged velocities we observe in the upper 10 km would require lower porosity, which could result from viscous closure of pore spaces due to thermal annealing expected to accompany volcanic resurfacing processes (*23, 39*), partial filling of pore spaces by the deposition of precipitated minerals from a briny ancient aquifer system (*40*), or the presence of a deep cryosphere or substantial water table beneath the thick Amazonian lava flows along the R1 path (*19, 41, 42*) (Fig. 3). We note that images from the High Resolution Imaging Science Experiment of the S1094b impact crater show large blocks of pure ice ejected from the shallower layers (*20*). This would not be expected to be the case near InSight, because the shallow crust with V_S of 1.7-2.1 km/s in the upper 8-11 km (*7*) rules out an ice-saturated cryosphere (*40*).

Another possibility is that a low density, high porosity layer beneath InSight results from ejecta deposited by the Utopia impact *(23)*. Because ejecta thickness is a strong function of radial distance, one would expect the ejecta thickness averaged along the R1 path to be much less than beneath InSight, consistent with the observations.

Regardless of the exact origin – composition and/or porosity – variations of crustal seismic structure presented here are likely correlated with density variations, because both temperature and compositional variations increase density together with V_S, and our results imply greater crustal densities between Elysium and Amazonis Planitiae than directly beneath the lander. This result is consistent with previous estimates of higher crustal density beneath the Elysium rise of 3100±100 kgm^{-3} (*43*) and lower density beneath the lander (*44*) from gravity-topography measurements. Density variations would also affect inferences of crustal thickness from topographic and gravity signals associated with the crustal dichotomy (*4, 23*). Currently, both exogenic (i.e., one or more large impacts; *45*) and endogenic (i.e., mantle convection) processes (*46*), or a combination thereof (*47*) continue to be debated as the origin of the dichotomy. Both processes would be expected to generate a basaltic secondary crust in the northern lowlands, consistent with the R1 observations from the two recent impacts. However, if confirmed by further analyses or other events, the S1094b R2 observation of similar group velocities across the southern hemisphere (once corrected for path in the Hellas impact basin) preliminarily indicates that the crustal structure at relevant depths could be substantially similar North and South of the dichotomy (Fig. 3).
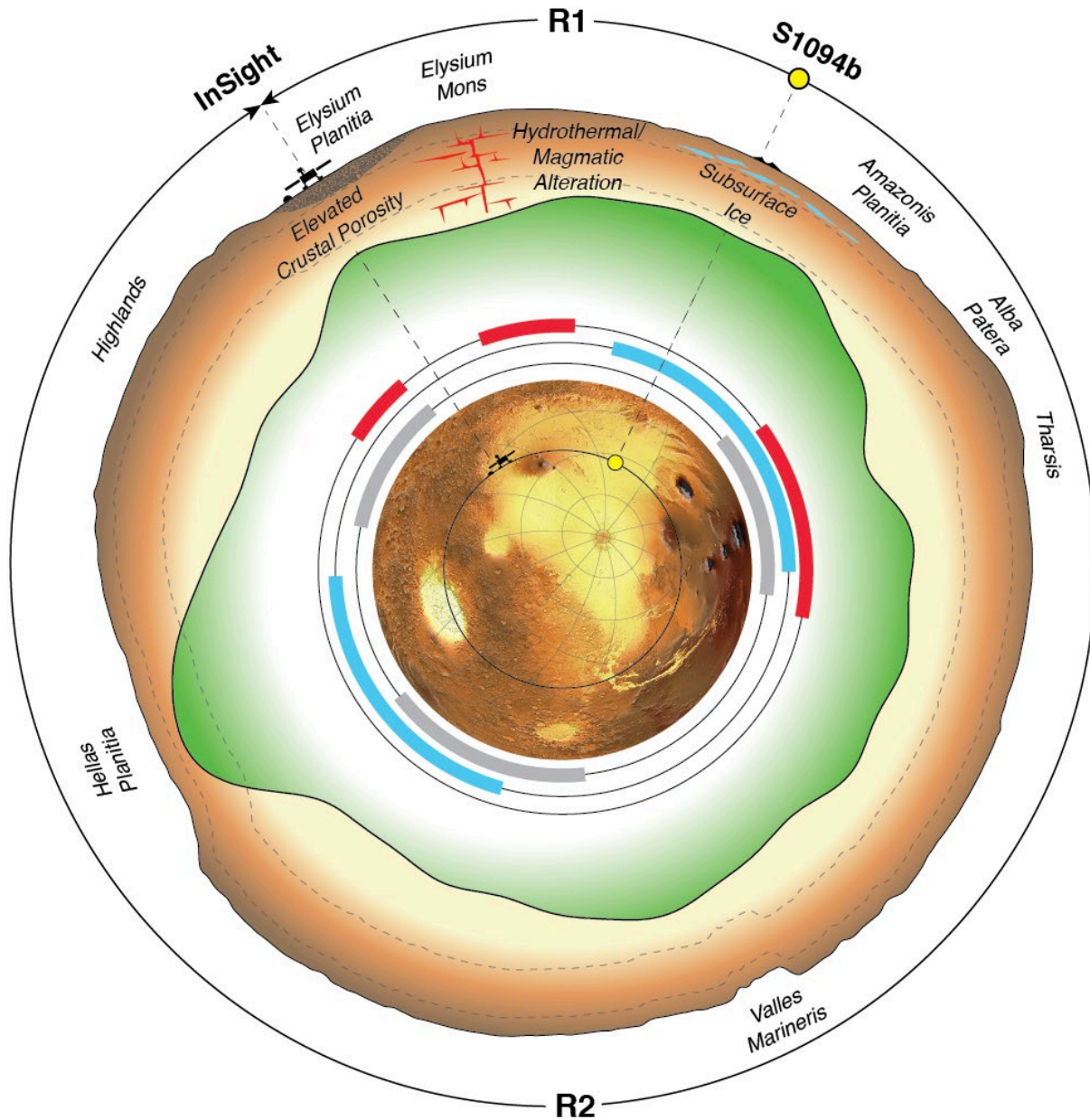
Figure 3. Cross section of the S1094b surface wave path through Mars. Surface topography (*21*) and crustal thickness (*23*) with a 20x vertical exaggeration are shown along the path of R1 and R2, with major geological provinces labeled at the surface and potential subsurface structures that affect surface wave velocity. The approximate sampling depth of the observed surface waves is indicated by gray dashed line. The inset context map shows the topography along the surface wave paths. The colored arcs indicate the path length(s) through provinces with surface volcanism (red), ice stability at latitudes > 30º (cyan), and cratered highlands (gray).

References and Notes

1. Taylor, S. R., & McLennan, S. M. (2009). Planetary crusts: Their composition, origin, nd evolution. Cambridge: Cambridge Univ. Press.
2. Smrekar, S.E., Lognonné, P., Spohn, T., Banerdt, W.B., Breuer, D., Christensen, U., Dehant, V., Drilleau, M., Folkner, W., Fuji, N. and Garcia, R.F., 2019. Pre-mission InSights on the interior of Mars. Space Science Reviews, 215(1), pp.1-72.
3. Zuber, M.T., 2001. The crust and mantle of Mars. Nature, 412(6843), pp.220-227.

4. Belleguic, V., Lognonné, P., Wieczorek, M., *Journal of Geophysical Research: Planets*, **110**(E11) (2005).

5. Banerdt, W. B., Smrekar, S. E., Banfield, D., Giardini, D., Golombek, M., Johnson, C. L., ... & Wieczorek, M. (2020). Initial results from the InSight mission on Mars. Nature Geoscience, 13(3), 183-189.

6. Lognonné, P., Banerdt, W.B., Pike, W.T., Giardini, D., Christensen, U., Garcia, R.F., Kawamura, T., Kedar, S., Knapmeyer-Endrun, B., Margerin, L. and Nimmo, F., 2020. Constraints on the shallow elastic and anelastic structure of Mars from InSight seismic data. Nature Geoscience, 13(3), pp.213-220.

7. Knapmeyer-Endrun, B., Panning, M.P., Bissig, F., Joshi, R., Khan, A., Kim, D., Lekić, V., Tauzin, B., Tharimena, S., Plasman, M. and Compaire, N., 2021. Thickness and structure of the martian crust from InSight seismic data. Science, 373(6553), pp.438-443.

8. Durán, C., Khan, A., Ceylan, S., Zenhäusern, G., Stähler, S., Clinton, J.F. and Giardini, D., 2022. Seismology on Mars: An analysis of direct, reflected, and converted seismic body waves with implications for interior structure. Physics of the Earth and Planetary Interiors, p.106851.

9. Kim, D., Lekić, V., Irving, J.C., Schmerr, N., Knapmeyer-Endrun, B., Joshi, R., Panning, M.P., Tauzin, B., Karakostas, F., Maguire, R. and Huang, Q., 2021. Improving constraints on planetary interiors with PPs receiver functions. Journal of Geophysical Research: Planets, 126(11), p.e2021JE006983.

10. Khan, A., Ceylan, S., van Driel, M., Giardini, D., Lognonné, P., Samuel, H., Schmerr, N.C., Stähler, S.C., Duran, A.C., Huang, Q. and Kim, D., 2021. Upper mantle structure of Mars from InSight seismic data. Science, 373(6553), pp.434-438.

11. Stähler, S.C., Khan, A., Banerdt, W.B., Lognonné, P., Giardini, D., Ceylan, S., Drilleau, M., Duran, A.C., Garcia, R.F., Huang, Q. and Kim, D., 2021. Seismic detection of the martian core. Science, 373(6553), pp.443-448.

12. Khan, A., Sossi, P. A., Liebske, C., Rivoldini, A., & Giardini, D. (2022). Geophysical and cosmochemical evidence for a volatile-rich Mars. *Earth and Planetary Science Letters*, 578, 117330.

13. Khan, A., van Driel, M., Böse, M., Giardini, D., Ceylan, S., Yan, J., ... & Banerdt, W. B. (2016). Single-station and single-event marsquake location and inversion for structure using synthetic Martian waveforms. Physics of the Earth and Planetary Interiors, 258, 28-42.

14. Toksöz, M.N. and Anderson, D.L., 1966. Phase velocities of long-period surface waves and structure of the upper mantle: 1. Great-Circle Love and Rayleigh wave data. Journal of Geophysical Research, 71(6), pp.1649-1658.

15. Böse, M., Stähler, S.C., Deichmann, N., Giardini, D., Clinton, J., Lognonné, P., Ceylan, S., van Driel, M., Charalambous, C., Dahmen, N. and Horleston, A., 2021. Magnitude scales for Marsquakes calibrated from InSight data. Bulletin of the Seismological Society of America, 111(6), pp.3003-3015.

16. Stutzmann, É., Schimmel, M., Lognonné, P., Horleston, A., Ceylan, S., van Driel, M., Stähler, S., Banerdt, B., Calvet, M., Charalambous, C. and Clinton, J., 2021. The polarization of ambient noise on Mars. Journal of Geophysical Research: Planets, 126(1), p.e2020JE006545.

17. van Driel, M., Ceylan, S., Clinton, J.F., Giardini, D., Horleston, A., Margerin, L., Stähler, S.C., Böse, M., Charalambous, C., Kawamura, T. and Khan, A., 2021. High-frequency seismic events on Mars observed by InSight. Journal of Geophysical Research: Planets, 126(2), p.e2020JE006670.

18. Dainty, A.M., Toksöz, M.N., Anderson, K.R., Pines, P.J., Nakamura, Y. and Latham, G., 1974. Seismic scattering and shallow structure of the Moon in Oceanus Procellarum. The Moon, 9(1), pp.11-29.

19. Materials and Methods are available as supplementary materials.

20. Posiolova et al., *Science*, in revision.

21. Smith, D.E., Zuber, M.T., Solomon, S.C., Phillips, R.J., Head, J.W., Garvin, J.B., Banerdt, W.B., Muhleman, D.O., Pettengill, G.H., Neumann, G.A. and Lemoine, F.G., 1999. The global topography of Mars and implications for surface evolution. science, 284(5419), pp.1495-1503.

22. Tanaka, K.L., Robbins, S.J., Fortezzo, C.M., Skinner Jr, J.A. and Hare, T.M., 2014. The digital global geologic map of Mars: Chronostratigraphic ages, topographic and crater morphologic characteristics, and updated resurfacing history. Planetary and Space Science, 95, pp.11-24.

23. Wieczorek, M. A., Broquet, A., McLennan, S. M., Rivoldini, A., Golombek M., Antonangeli, D., Beghein, C., Giardini, D., Gudkova, T., … 2022. InSight constraints on the global character of the Martian crust, Journal of Geophysical Research: Planets, in press, doi:10.5281/zenodo.4439426.

24. Kim, D., Davis, P., Lekić, V., Maguire, R., Compaire, N., Schimmel, M., Stutzmann, E., CE Irving, J., Lognonné, P., Scholz, J.R. and Clinton, J., 2021. Potential pitfalls in the analysis and structural interpretation of seismic data from the Mars InSight mission. Bulletin of the Seismological Society of America, 111(6), pp.2982-3002.

25. Giardini, D., Lognonné, P., Banerdt, W.B., Pike, W.T., Christensen, U., Ceylan, S., Clinton, J.F., van Driel, M., Stähler, S.C., Böse, M. and Garcia, R.F., 2020. The seismicity of Mars. Nature Geoscience, 13(3), pp.205-212.

26. Garcia, R. F., Murdoch, N., Lorenz, R., Spiga, A., Bowman, D. C., Lognonné, P., ... & Banerdt, W. B. (2021). Search for infrasound signals in InSight data using coupled pressure/ground deformation methods. Bulletin of the Seismological Society of America, 111(6), 3055-3064.

27. Moulik, P., Lekic, V., Romanowicz, B., Ma, Z., Schaeffer, A., Ho, T., Beucler, E., Debayle, E., Deuss, A., Durand, S. and Ekström, G., 2022. Global reference seismological data sets: multimode surface wave dispersion. Geophysical Journal International, 228(3), pp.1808-1849.

28. Wieczorek, M. A., & Phillips, R. J. (1999). Lunar multiring basins and the cratering process. Icarus, 139(2), 246-259.

29. Platz, T., & Michael, G. (2011). Eruption history of the Elysium volcanic province, Mars. Earth and Planetary Science Letters, 312(1-2), 140-151.

30. Golombek, M., Grott, M., Kargl, G., Andrade, J., Marshall, J., Warner, N., ... & Banerdt, W. B. (2018). Geology and physical properties investigations by the InSight lander. Space Science Reviews, 214(5), 1-52.

31. Golombek, M., Warner, N. H., Grant, J. A., Hauber, E., Ansan, V., Weitz, C. M., ... & Banerdt, W. B. (2020). Geology of the InSight landing site on Mars. Nature communications, 11(1), 1-11.

32. Pan, L., Quantin-Nataf, C., Tauzin, B., Michaut, C., Golombek, M., Lognonné, P., ... & Lucas, A. (2020). Crust stratigraphy and heterogeneities of the first kilometers at the dichotomy boundary in western Elysium Planitia and implications for InSight lander. Icarus, 338, 113511.

33. Baratoux, D., Samuel, H., Michaut, C., Toplis, M. J., Monnereau, M., Wieczorek, M., ... & Kurita, K. (2014). Petrological constraints on the density of the Martian crust. Journal of Geophysical Research: Planets, 119(7), 1707-1727.

34. Wilson, L. and Head, J. W. III (1994) Mars: Review and analysis of volcanic eruption theory and relationships to observed landforms. Rev. Geophys., 32, 221-263.

35. Christiansen, E. H., Best, M. G. and Radebaugh, J. (2022) The origin of magma on planetary bodies. In: T. K. P. Gregg, R. M. C. Lopes and S. A. Fagents (Eds.) Planetary Volcanism Across the Solar System (Elsevier, Amsterdam) pp. 235-270.

36. Taylor, G. J. (2013). The bulk composition of Mars. Geochemistry, 73(4), 401-420.

37. Black, B. A., & Manga, M. (2016). The eruptibility of magmas at Tharsis and Syrtis Major on Mars. Journal of Geophysical Research: Planets, 121(6), 944-964.

38. McCubbin, F. M., Nekvasil, H., Harrington, A. D., Elardo, S. M., Lindsley, D. H., J. Geophys. Res. – Planets, 113, E11013 (2008).

39. Gyalay, S., Nimmo, F., Plesa, A. C., Wieczorek, M., *Geophysical Research Letters*, **47**(16), e2020GL088653 (2020).

40. Manga, M. and Wright, V., 2021. No cryosphere-confined aquifer below InSight on Mars. Geophysical Research Letters, 48(8), p.e2021GL093127.

41. Clifford, S. M., Lasue, J., Heggy, E., Boisson, J., McGovern, P., & Max, M. D. (2010). Depth of the Martian cryosphere: Revised estimates and implications for the existence and detection of subpermafrost groundwater. Journal of Geophysical Research: Planets, 115(E7).

42. De Toffoli, B., Massironi, M., Mazzarini, F., & Bistacchi, A. (2021). Rheological and Mechanical Layering of the Crust underneath thumbprint terrains in Arcadia Planitia, Mars. Journal of Geophysical Research: Planets, 126(11), e2021JE007007.

43. Broquet, A., Wieczorek, M. A., *Journal of Geophysical Research: Planets*, **124**(8), 2054-2086 (2019).

44. Gudkova, T. V., Stepanova, I. E., & Batov, A. V. (2020). Density anomalies in subsurface layers of mars: Model estimates for the site of the InSight mission seismometer. Solar System Research, 54(1), 15-19.

45. Andrews-Hanna, J.C., Zuber, M. T., and Banerdt, W. B., (2008). The Borealis Basin and the Martian crustal dichotomy, Nature, 453, 1212-1215.

46. Nimmo, F. and Tanaka, K., 2005. Early crustal evolution of Mars. Annu. Rev. Earth Planet. Sci., 33, pp.133-161.

47. Citron, R.I., Manga, M. and Hemingway, D.J., 2018. Timing of oceans on Mars from shoreline deformation. Nature, 555(7698), pp.643-646.

48. InSight Marsquake Service (2022). Mars Seismic Catalogue, InSight Mission; V11 2022-07-01. ETHZ, IPGP, JPL, ICL, Univ. Bristol. https://doi.org/10.12686/a17

49. InSight Mars SEIS Data Service (2019). InSight SEIS Data Bundle. PDS Geosciences (GEO) Node, doi: 10.17189/1517570.

50. InSight Mars SEIS Data Service (2019). SEIS raw data, InSight Mission. IPGP, JPL, CNES, ETHZ, ICL, MPS, ISAE-Supaero, LPG, MFSC. http://doi.org/10.18715/SEIS.INSIGHT.XB_2016.

51. Lognonné, P., Banerdt, W. B., Giardini, D., Pike, W. T., Christensen, U., Laudet, P., ... & Berenguer, J. L. (2019). SEIS: Insight's seismic experiment for internal structure of Mars. Space Science Reviews, 215(1), 1-170.

52. Horleston et al., (2022). The far side of Mars: two distant marsquakes detected by InSight, The Seismic Record, 2 (2): 88-99.

53. Charalambous, C., Stott, A. E., Pike, T., McClean, J. B., Warren, T., Spiga, A., ... & Banerdt, W. B. (2021). A comodulation analysis of atmospheric energy injection into the ground motion at InSight, Mars. Journal of Geophysical Research. Planets.

54. Scholz, J. R., Widmer-Schnidrig, R., Davis, P., Lognonné, P., Pinot, B., Garcia, R. F., ... & Banerdt, W. B. (2020). Detection, analysis, and removal of glitches from InSight's seismic data from Mars. Earth and Space Science, 7(11), e2020EA001317.

55. Park, J., Vernon III, F. L., and C. R. Lindberg, Frequency dependent polarization analysis of high-frequency seismograms. *Journal of Geophysical Research: Solid Earth*, 92 (B12), pp. 12664-12674 (1987).

56. Clinton, J. F., Ceylan, S., van Driel, M., Giardini, D., Stähler, S. C., Böse, M., ... & Stott, A.

E. (2021). The Marsquake catalogue from InSight, sols 0–478. Physics of the Earth and Planetary Interiors, 310, 106595.

57. Ceylan, S., Clinton, J. F., Giardini, D., Böse, M., Charalambous, C., Van Driel, M., ... & Perrin, C. (2021). Companion guide to the marsquake catalog from InSight, Sols 0–478: Data content and non-seismic events. Physics of the Earth and Planetary Interiors, 310, 106597.

58. Dahmen, N. L., Zenhäusern, G., Clinton, J. F., Giardini, D., Stähler, S. C., Ceylan, S., ... & Banerdt, W. B. (2021). Resonances and lander modes observed by insight on Mars (1–9 Hz). Bulletin of the Seismological Society of America, 111(6), 2924-2950.

59. Poppeliers C., and Preston L. 2019. The use of multiwavelets to quantify the uncertainty of single-station surface wave dispersion estimates, Seismol. Res. Lett. 90, no. 2A, 754–764, doi: https://doi.org/10.1785/0220180145.

60. Preston, L., Poppeliers, C., & Schodt, D. J. (2020). Seismic Characterization of the Nevada National Security Site Using Joint Body Wave, Surface Wave, and Gravity Inversion Seismic Characterization of the NNSS Using Joint Body Wave, Surface Wave, and Gravity Inversion. Bulletin of the Seismological Society of America, 110(1), 110-126.

61. Dziewonski, A., Bloch, S., & Landisman, M. (1969). A technique for the analysis of transient seismic signals. Bulletin of the seismological Society of America, 59(1), 427-444.

62. Meier, T., Dietrich, K., Stöckhert, B., & Harjes, H. P. (2004). One-dimensional models of shear wave velocity for the eastern Mediterranean obtained from the inversion of Rayleigh wave phase velocities and tectonic implications. Geophysical Journal International, 156(1), 45-58.

63. Levshin, A. L., Ritzwoller, M. H., & Resovsky, J. S. (1999). Source effects on surface wave group travel times and group velocity maps. Physics of the Earth and Planetary Interiors, 115(3-4), 293-312.

64. Laske, G., and Widmer-Schnidrig, R., (2015). Theories and Observations: Normal Mode and Surface Wave Observations. Treaties on Geophysics, http://dx.doi.org/10.1016/B978-0-444-53802-4.00003-8

65. Sambridge, Malcolm, and Klaus Mosegaard. "Monte Carlo Methods in Geophysical Inverse Problems." *Reviews of Geophysics* 40, no. 3 (2002): 3-1-3–29. https://doi.org/10.1029/2000RG000089.

66. Jiang, Chengxin, Brandon Schmandt, Jamie Farrell, Fan Chi Lin, and Kevin M. Ward. "Seismically Anisotropic Magma Reservoirs Underlying Silicic Calderas." *Geology* 46, no. 8 (2018): 727–30. https://doi.org/10.1130/G45104.1.

67. Kennett, B. L. N. (1991). The removal of free surface interactions from three-component seismograms. Geophysical Journal International, 104(1), 153-163.

68. Christensen, Nikolas I, and Walter D Mooney. "Seismic Velocity Structure and Composition of the Continental Crust: A Global View." *Journal of Geophysical Research: Solid Earth* 100, no. B6 (1995): 9761–88.

69. Herrmann, Robert B. "Computer Programs in Seismology: An Evolving Tool for Instruction and Research." *Seismological Research Letters* 84, no. 6 (2013): 1081–88. https://doi.org/10.1785/0220110096.

70. Hastings, W Keith. "Monte Carlo Sampling Methods Using Markov Chains and Their Applications." *Biometrika* 57 (1970): 97–109.

71. Drilleau, M., Beucler, E., Mocquet, A., Verhoeven, O., Moebs, G., Burgos, G., ... & Vacher, P. (2013). A Bayesian approach to infer radial models of temperature and anisotropy in the transition zone from surface wave dispersion curves. Geophysical Journal International, 195(2), 1165-1183.

72. Drilleau, M., Samuel, H., Rivoldini, A., Panning, M., & Lognonné, P. (2021). Bayesian

inversion of the Martian structure using geodynamic constraints. Geophysical Journal International, 226(3), 1615-1644.

73. Birch, F. (1961). The velocity of compressional waves in rocks to 10 kilobars: 2. Journal of Geophysical Research, 66(7), 2199-2224.

74. Malinverno, A. (2002). Parsimonious Bayesian Markov chain Monte Carlo inversion in a nonlinear geophysical problem. Geophysical Journal International, 151(3), 675-688.

75. Gao, C., & Lekić, V. (2018). Consequences of parametrization choices in surface wave inversion: Insights from transdimensional Bayesian methods. Geophysical Journal International, 215(2), 1037-1063.

76. Masters, G., Woodhouse, J. H., & Freeman, G. (2011). Mineos v1. 0.2 [software], computational infrastructure for geodynamics. Available from: geodynamics. org, doi: NoDOI, url: https://geodynamics. org/cig/software/mineos.

77. Weidner, E., Beghein, C., Huang, Q., and Schmerr, N., 2021. Upper mantle radial anisotropy under the Indian Ocean from higher mode surface waves and a hierarchical transdismensional approach, Geophys. J. Int., 228, 78-101.

78. Koper, K.D., Wysession, M.E. & Wiens, D.A., 1999. Multimodal function optimization with a niching genetic algorithm: a seismological example, Bull. seism. Soc. Am., 89(4), 978–988.

79. Li, J., Chen, M., Koper, K.D., Zhou, T., Xi, Z., Li, S. & Li, G., 2021. FastTrip: a fast MPI-accelerated 1D triplication waveform inversion package for constraining mantle transition zone discontinuities, Seismol. Res. Lett., 92(4), 2647–2656.

80. Dou, S., & Ajo-Franklin, J. B. (2014). Full-wavefield inversion of surface waves for mapping embedded low-velocity zones in permafrost. Geophysics, 79(6), EN107-EN124.

81. Schmerr, N. C., Banks, M. E., & Daubar, I. J. (2019). The seismic signatures of recently formed impact craters on Mars. Journal of Geophysical Research: Planets, 124(11), 3063-3081.

82. Maupin, V. (2017). 3-D sensitivity kernels of the Rayleigh wave ellipticity. Geophysical Journal International, 211(1), 107-119.

83. Lin, F. C., Tsai, V. C., & Schmandt, B. (2014). 3-D crustal structure of the western United States: application of Rayleigh-wave ellipticity extracted from noise cross-correlations. Geophysical Journal International, 198(2), 656-670.

84. Park, J., Lindberg, C. R., & Vernon III, F. L. (1987). Multitaper spectral analysis of high-frequency seismograms. Journal of Geophysical Research: Solid Earth, 92(B12), 12675-12684.

85. Tanimoto, T., & Rivera, L. (2008). The ZH ratio method for long-period seismic data: sensitivity kernels and observational techniques. Geophysical Journal International, 172(1), 187-198.

86. Dahlen, F. A., Tromp, J. (1998). Theoretical Global Seismology, Princeton University Press, Princeton, New Jersey

87. Ligorria, J. P., & Ammon, C. J., Iterative deconvolution and receiver-function estimation. Bulletin of the seismological Society of America , 89(5):1395–1400, 1999.

88. Kind, R., Kosarev, G. L., & Petersen, N. V. (1995). Receiver functions at the stations of the German Regional Seismic Network (GRSN). Geophysical Journal International, 121(1), 191-202.

89. Te Wu, T. (1966). The effect of inclusion shape on the elastic moduli of a two-phase material. International Journal of solids and structures, 2(1), 1-8.

90. Toksöz, M. N., Cheng, C. H., & Timur, A. (1976). Velocities of seismic waves in porous rocks. Geophysics, 41(4), 621-645.

91. Heap, M. J. (2019). P-and S-wave velocity of dry, water-saturated, and frozen basalt:

Implications for the interpretation of Martian seismic data. Icarus, 330, 11-15.

Supplementary Materials

Materials and Methods

Supplementary Text

Figs. S1 to S21

References (*51–91*)